eprints@whiterose.ac.uk
https://eprints.whiterose.ac.uk/

Electromagnetic-thermal Coupled Simulation under Various Fault Conditions of a Triple Redundant 9-phase PMASynRM

Yanwen Shi, Jiabin Wang, Senior Member, *IEEE*, and Bo Wang, Member, *IEEE*

Abstract—This paper performs electromagnetic (EM) and thermal coupled simulation based on 2D transient electromagnetic and 3D thermal model of a triple redundant 9-phase permanent magnet-assisted synchronous reluctance motor (PMASynRM) under various fault conditions at different speeds. The coupled simulation process is controlled by a scripting file. The resultant temperatures under EM-thermal coupled simulation will be comprehensively compared with those under thermal-only simulation. The predicted current waveforms under fault conditions by the 2D EM model and predicted temperatures by the 3D thermal model will be compared with the test results for validation. The outcomes of the study not only gives a better understanding of the thermal behavior, but also provides a guidance to the necessity of the EM-thermal coupled simulation under different fault conditions as well as to determination of the maximum permissible fault detection time before permanent damage due to the fault may occur.

Index Terms— Permanent magnet-assisted synchronous reluctance motor, EM-thermal coupled simulation, fault condition, temperature distribution, detection time, resistance limited, reactance limited.

I. INTRODUCTION

TEMPERATURE is one of the key constraints to ensure the fault tolerant machine's safety and reliability in safety critical applications, such as "All Electric Aircraft" and "More Electric Aircraft", because the insulation life decreases significantly when the winding temperature is beyond a permissible limit[1]. Therefore, it is vital to develop an accurate thermal analysis at design stage to predict the temperature distribution and hotspot temperature both under healthy and fault conditions.

Usually, losses obtained from electromagnetic (EM) model are simply fed to a lumped parameter (LP) thermal model or commercial finite element (FE) tools to obtain the temperature distribution[2, 3]. Copper loss variation with temperature can be accounted under the assumption that the machine current and back electromotive force (EMF) are independent of temperature. However, this assumption may not be valid for synchronous reluctance machines equipped with permanent magnets as the flux produced by the magnets may strongly depend on temperature. The work described in [4, 5] combines the EM model with a LP thermal model through iterative data exchange for predicting the steady-state average temperature in different parts of a machine when the assumption is no longer true. The technique is computationally efficient, but less accurate. Therefore, finite element (FE) based EM model combined with a FE based or computational fluid dynamics (CFD) based thermal model are employed in co-simulations in [6-8]. However, the two models are not directly connected and the data exchange is manual. While the methods are more accurate, they are time consuming and inefficient.

Very few existing papers have considered the directly coupled EM-thermal simulation based on the FE transient models because of the complexity and different time constants between two physical fields. Moreover, fewer have considered coupled EM-thermal simulations under fault conditions. However, EM-thermal coupled simulation is significantly vital under fault conditions, especially when the current is not known and dependent on the EM behavior of the machine. Moreover, under some fault conditions, temperature effects on the winding resistance may have a significant influence on the magnetic field and resultant fault current, such as under inter-turn short circuit fault [9].

As discussed in [9], firstly, the phase resistance is the dominant component of the phase impedance when a small number of turns are short-circuited or the machine operates at low speed, leading to overestimates of the temperature rise and steady-state temperatures if the temperature effect on resistivity is neglected. When a large number of turns are short-circuited or the machine operates at high speed, the resistive and reactive components of a faulted winding may be similar or the reactance may become dominant. In both cases the resistance increase with temperature has little effect on current while the copper loss increases with temperature. Consequently, the temperature increases faster and reaches a higher value than the prediction without considering the temperature effect. Therefore, it is essential to perform EM-thermal coupled simulation for accurate prediction of the fault behavior. Additionally, it is also necessary to accurately assess the maximum permissible time for fault detection and mitigation before the winding temperature reaches a point beyond which a catastrophic failure may occur.

This paper performs a directly coupled EM-thermal simulation based on 2D transient EM and 3D thermal model of a triple redundant, 9-phase (3x3-phase), PMASynRM reported

in [10]. A scripting file will be used to exchange data during each step to predict the temperature distribution under various faults at different speeds. The transient temperature results under EM-thermal coupled simulation will be comprehensively compared with those under thermal-only simulation with constant losses. Additionally, the current waveforms under fault conditions predicted by the 2D EM model and temperatures predicted by the 3D thermal model will be compared with the test results to validate the two models, respectively. The paper also discusses the necessity of the EM-thermal coupled simulation against different fault conditions and quantities the maximum permissible fault detection time for the worst case, under one turn short circuit at the rated torque and base speed of 4000rpm.

II. EM-THERMAL COUPLED SIMULATION

A. The Process of Coupled Simulation

The EM-thermal coupled simulation will be performed in JMAG by two steps, as shown in Fig. 1 [9] [11]. Fig. 1 (a) shows the flowchart of Step 1 to predict the temperature distribution under healthy condition. As observed, the initial temperature will be assigned to the 2D transient EM and 3D static thermal models at the beginning. Then, the material properties and resistance of the winding in the EM model can be updated with temperature after each iteration. The calculated losses obtained from the EM model and steady-state temperatures gathered from the thermal model will be exchanged iteratively. When the temperature results satisfy the convergence criterion that the maximum residual should be less than 0.1°C, the final temperature distribution under healthy condition is obtained.
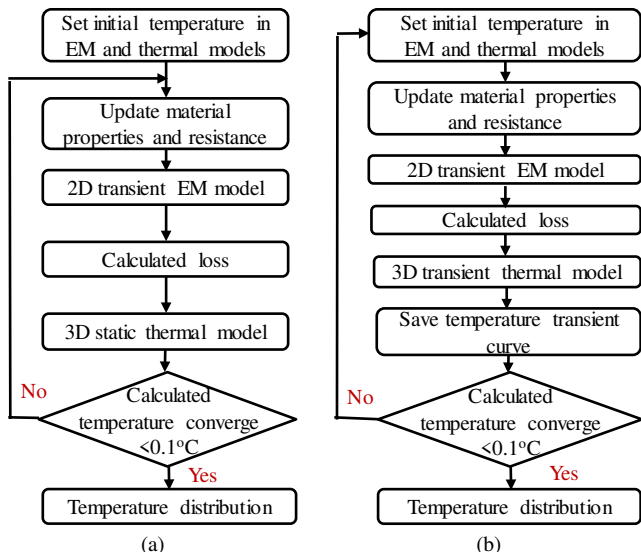

Fig. 1. Flowchart of EM-thermal coupled simulation. (a) Step 1: healthy condition. (b) Step 2: fault condition.

Fig. 1 (b) shows the flowchart of Step 2 to predict the temperature distribution under fault condition. The whole process is divided into a number of appropriate steps. Firstly, the healthy temperature distribution in Step 1 will be extracted and assigned as the initial temperature to the 2D EM model and

the 3D transient thermal model. Subsequently, the temperature-dependent material properties and resistances will be updated in the EM model. The new losses predicted by the EM model are fed to the 3D thermal model that in turn predicts new temperature distribution at the end of the time step. The temperature distribution will be checked for convergence with those predicted in the previous step. If a convergence criterion is not met, the temperatures will be fed to the EM and the thermal models as the new initial temperature. The process will repeat until convergence. When the results converge, the transient temperature rise of every step can be extracted. All the coupled simulation processes are controlled by a scripting file.

B. 2D Electromagnetic and 3D Thermal Models

A triple redundant, 9-phase (3x3-phase), 36-slot, 6-pole PMASynRM as shown in Fig. 2 has high saliency leading to low permanent magnet usage and inherent large reluctance torque. It exhibits comparable performance with conventional PM machines in terms of efficiency (95.8%) and torque density (34.2kNm/m^3) [10]. The low PM field results in low back EMF and low SC current with improved fault tolerance. Additionally, as in Fig. 2 (b), the machine employs three 3-phase sets that each 3-phase set does not overlap with the other sets to improve the physical and thermal isolations between the different 3-phase sets compared with the conventional overlapped distributed windings. The three 3-phase sets are denoted as ABC, DEF and GHI. In addition, each 3-phase set is controlled by an independent 3-phase inverter for electrical isolation. Thus, fault propagation between different 3-phase sets is minimized. It has been demonstrated in [10] and [12] that the machine has excellent fault tolerant capability under many common faults, including the open-circuit, intra-phase (inter-turn SC within a phase) SC and inter-phase SC, uncontrolled rectification at high speed due to inverter failure, DC capacitor fault and demagnetization under voltage reversal fault. However, it is important to gain in-depth understanding of the thermal characteristics of this machine in fault conditions.
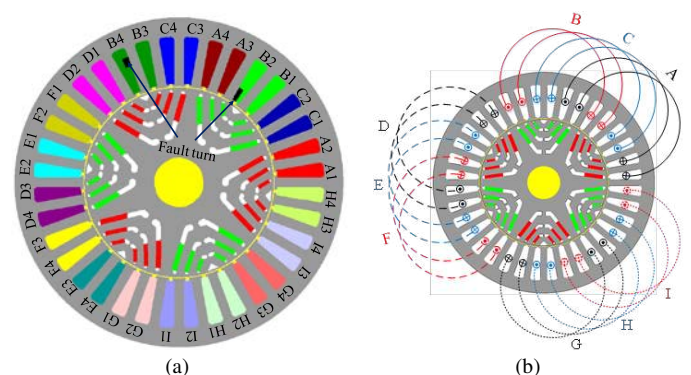

Fig. 2. Cross section of a triple redundant, 9-phase PMASynRM. (a) Named slots and short-circuit turn. (b) Layout of windings.

The permanent magnet material is VACOMAX 225 HR, while the stator and rotor materials are 0.2mm Vacoflux 50 and Vacodur 50, respectively. Eddy current loss in magnets (27.9W), iron loss (307W) and copper loss (1100W) are

predicted by the 2D EM model at 20°C. Therefore, the eddy current loss in the magnets only accounts for about 2% of the total loss. The hysteresis loss dominating the iron loss (73%) at the operating speed does not vary essentially with temperature [13]. Moreover, the temperature coefficient of the conductivity of the core material is much lower than the copper. Thus, the iron loss and eddy current loss are considered independent of temperature while the temperature-dependent copper loss is accounted during the coupled simulation. The machine employs single layer winding with 2 series connected coils per phase, as shown in Fig. 2 (b) and each coil has 8 turns.

The 1/3 3D model encompassing 12 slots and half of the machine axial length with symmetric boundary condition and the schematic heat transfer network illustrated in Figs. 3 and 4, respectively, form the complete thermal model of this motor in JMAG [11]. As well known, when the heating effect and temperature distribution in the three 3-phase winding sets are very asymmetric in the thermal analysis, such as one turn SC with 3-phase terminal SC, the full 3D thermal model is more accurate than the 1/3 model. However, the 1/3 model is usually adopted when the machine is healthy or when the heating effect of the fault is localized and is less significant compared to the total of the machine under a given load condition, or over a short duration in which the heat is more likely to be stored in the materials than dissipate to other regions. As this section focuses on the performance compared between two simulation methods on the same 3D thermal model, the 1/3 model is adopted under all fault conditions due to smaller size and computationally less demanding with reasonable accuracy.

The windings are potted and composed of conductor and Stycast 2676FT. From Fig. 2, the winding layout is quite complex to represent in the 3D model. Further, because the copper loss and temperature distribution in the healthy and faulted turns are different, the end winding part cannot be simplified as a homogeneous ring. Thus, the end winding is simplified in the 3D thermal model as straight winding segments with the same equivalent length as those in the prototype machine and the thermal coupling between two different phases in the end winding is represented by the potting composed of pure Stycast 2676FT as illustrated Fig. 3.
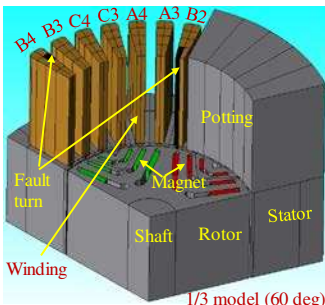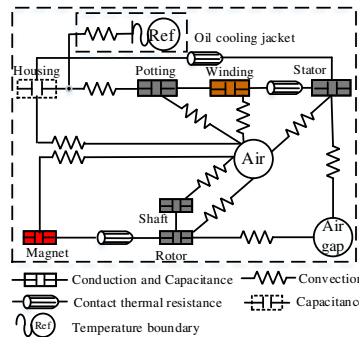

Fig. 3. 1/3 3D thermal model.

Fig. 4. Schematic diagram of heat equivalent circuit of this motor.

The commercial software package, Motor-CAD, [14] as well as empirical equations [15] are used to help build the model. Radiation heat transfer is negligible in the study because of the small temperature difference between the machine surfaces and ambient.

Furthermore, heat conductions and thermal capacitances in various components of the machine, such as potting, stator, rotor, magnet and shaft, are predicted in the 3D thermal model when thermal conductivities and heat capacities are appropriately set [16]. The contact thermal resistances that are dependent on the gap thickness and the thermal conductivity of the interface material are appropriately modelled. These include the resistance between the winding and stator core, the magnet and rotor core, and the stator core and housing. The oil cooling jacket is represented as a temperature boundary with an equivalent convection resistance between the stator cooling channels and cooling oil in the 3D thermal model [17].

The convective thermal resistance R_c for a given cooling condition can be estimated by the commercial package [14] and convection coefficient h_c is estimated in (1) with known surface area A_c:

$$h_c = 1/R_c A_c \qquad (1)$$

Convective thermal resistances in the airgap and between various parts and air are similarly estimated for setting up convection boundary conditions in the 3D thermal model.

Electrical winding is a critical part in the thermal model as it has high heat flux density. Thus, it is very important to calculate the thermal parameters of windings which usually consist of conductors, wire insulations and impregnations. The equivalent thermal conductivity using analytical homogenization is employed. However, it is worth noting that the equivalent thermal conductivity is significantly different in the axial and radial or circumferential directions. Usually, the axial thermal conductivity is far larger than the radial thermal conductivity, so the coil loss is easily transferred in the axial direction.

It is assumed that the winding only consists of two materials, the conductor and the impregnation which is Stycast 2676FT as the volume of the wire insulation is much smaller than that of the impregnation. Thus, the Hashin and Shtrickman approximation [18] which has been validated experimentally in a number of papers [19-20] can be used to estimate the radial/circumferential equivalent thermal conductivity $k_{rad/cir}$:

$$k_{rad/cir} = k_p \frac{(1+v_c)k_c + ((1-v_c)k_p}{(1-v_c)k_c + ((1+v_c)k_p} \qquad (2)$$

where k_c and k_p is the copper and impregnation thermal conductivity, respectively; and v_c is the copper slot fill factor.

The axial equivalent thermal conductivity k_{axial} is simply calculated from the parallel model [20] for two materials given in (3):

$$k_{axial} = v_c k_c + (1-v_c)k_p \qquad (3)$$

The equivalent specific heat capacity c_e of the coil also combines the effect of conductors and impregnations as given by [20]:

$$c_e = \frac{v_c(\rho_c c_c - \rho_p c_p) + \rho_p c_p}{v_c(\rho_c - \rho_p) + \rho_p} \qquad (4)$$

where c_c and ρ_c is the specific heat capacity and mass density of the copper, respectively; c_p and ρ_p is the specific heat capacity and mass density of the impregnation, respectively.

III. THERMAL BEHAVIOR UNDER VARIOUS FAULT CONDITIONS

The temperature distribution of the machine under healthy condition with the rated current of 120A at 500rpm and 4000rpm are predicted and compared with the results obtained from the commercial package [14], [9]. Therefore, the good agreement between the two predictions shows the 3D thermal simulation being correctly performed. Then, the temperature distributions in healthy conditions are extracted as the initial temperatures for simulations in fault conditions. Four fault conditions considered in this paper are listed in Table I. F1 and F2 represent a single turn SC at two different speeds. F3 is performed to study the influence of number of SC turns on thermal behavior, and F4 represents the remedial action. As described previously, SC current may be mainly limited by the resistance when a small number of turns are SC or at low speed. However, for this machine at the rated speed of 4000rpm, the SC current is reactance limited with one or two SC turns. In contrast case F1 is resistance limited because of low speed. In all four conditions, the currents in healthy phases are set to the rated value with phase angle for maximum torque per Ampere operation.

TABLE I
FAULT CONDITIONS UNDER CONSIDERATION.

Fault name	Discription
F1	One turn SC at 500 rpm
F2	One turn SC at 4000 rpm
F3	Two turns SC at 4000 rpm
F4	One turn SC with 3-phase terminal SC at 4000 rpm

All the faults are assumed to occur in phase B of the 3-phase set ABC. Thus, phase B is divided into the healthy part denoted as Phase_B_healthy and the fault part denoted as SC turn. As the machine has triple 3-phase sets, the mutual coupling between the two healthy 3-phase sets and one faulty 3-phase set will influence the fault current and resultant copper loss. It has been shown in [21] that when a turn-to-turn SC located in slot B2 and slot B4 which are marked by the two black quadrangles shown in Fig. 2 (a) takes place, the SC current and copper loss are the highest.

The coupled simulation under the fault conditions is divided into 49 steps. As temperature increases dramatically at the beginning when the fault occurs and changes much slowly in the late stage, the time step is varied. In the first 30 steps, a time interval of 2s is used, while in the last 19 steps, 40s is used in each step. Thus, the total simulation time is 820s and the computation time is 8h48min in a typical PC. For the purpose comparison, the thermal behavior under the same fault is also predicted by the thermal model without account of temperature influence on electromagnetic behavior and the computation time is 5min in a typical PC.

A. Fault Behavior under F1

Fault F1 is one turn SC at 500 rpm in which the resistance dominates the fault turn impedance. It is shown in Fig. 5 that the copper loss in the SC turn reduces with the time and increased temperature. The transient hotspot temperature rise predicted by the EM-thermal coupled simulation is compared with that predicted by thermal-only simulation in Fig. 5.

As observed, the differences between two methods are quite small because the SC current at 500rpm and, hence, the copper loss of the SC turn is relatively small which accounts for smaller than 10% of the total copper loss. With increase in temperature when the fault occurs, the SC current decreases, resulting in lower temperature than that when the influence of temperature on the fault current is neglected. Thus, the EM-thermal coupled simulation improves slightly prediction accuracy under the resistance limited condition at low speed.
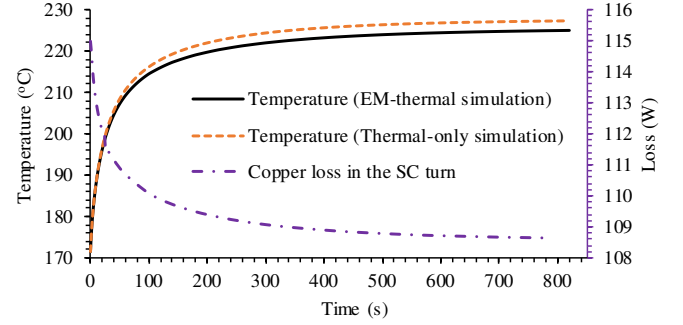

Fig. 5. SC turn loss and comparison of the hotspot temperature with time under F1.

B. Fault Behavior under F2

Fault F2 is one turn SC at 4000 rpm in which the SC current is extremely high and is largely dependent on the reactance of the short-circuit path. Hence, the resultant loss in the SC turn accounting for about 37% of the total copper loss increases dramatically with both increases in temperature and in the turn resistance. The temperature distributions of the faulted ABC 3-phase set at 820s under F2 predicted by the two simulation methods are shown in Fig. 6 in the same range of temperature scaling. As observed from Fig. 6, the hotspot is located in the end winding part of the SC turn near the slot opening. It is evident that the temperatures predicted by the EM-thermal coupled simulation are much higher, especially in the regions close to the SC turn than those by the thermal-only simulation.
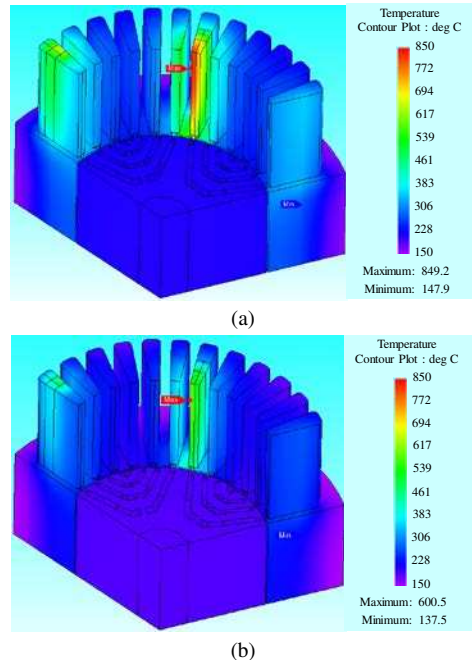

Fig. 6. Temperature distribution under F2 at 820s between two simulated methods. (a) EM-thermal coupled simulation. (b) Thermal-only simulation.

Fig. 7 and Table II compare the transient hotspot temperature over the time duration of 820s, and the temperature distributions in different parts of the machine at 820s, respectively. As observed, the thermal-only simulation underestimates the temperatures in all parts significantly. Besides, the underestimate of the hotspot temperature becomes larger with increase in time and reaches (249°C) at 820s as shown in Fig. 7. The comparison demonstrates the necessity of the EM-thermal coupled simulation under F2.
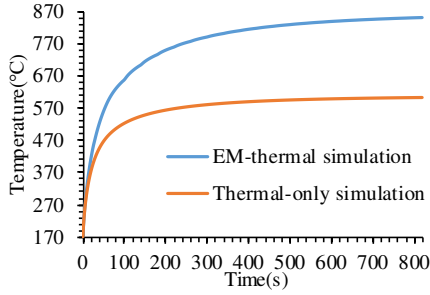

Fig. 7. Comparison of hotspot temperature between two simulated methods under F2.

TABLE II
COMPARISONS OF TEMPERATURE VALUES AT 820S UNDER F2

Component temperature	EM-thermal	Thermal-only	Difference
Rotor (°C)	217	194	22
Shaft (°C)	213	193	21
Magnet (°C)	218	195	23
Stator (°C)	209	180	29
Phase A (°C)	265	220	45
Phase C (°C)	228	197	31
Phase B healthy (°C)	350	274	77
SC turn (°C)	608	441	167
Hotspot (°C)	849	601	249

C. Fault Behavior under F3

Two turns SC fault at 4000 rpm, denoted as F3, is also simulated. The turn fault current is lower than that under F2 due to increase in inductance of the fault path that is proportional to the square of the number of the SC turns. Under this condition, the SC current is also reactance dominant, and hence the copper loss in the SC turn accounting for about 30% of the total copper loss increases with both increases in temperature and the faulted turn resistances. Table III compares the temperature distributions in different parts of the machine at 820s.

The resultant temperatures predicted by the EM-thermal coupled simulation are also much greater than those by the thermal-only simulation albeit the temperatures of the machine under F3 are much lower than those under F2. This means that the two turns SC is less severe than one turn SC in this machine with two series connected coils per phase and each coil having 8 turns.

TABLE III
COMPARISONS OF TEMPERATURE VALUES AT 820S UNDER F3

Component temperature	EM-thermal	Thermal-only	Difference
Rotor (°C)	198	183	15
Shaft (°C)	196	182	14
Magnet (°C)	199	184	15
Stator (°C)	187	166	21
Phase A (°C)	232	200	32
Phase C (°C)	206	184	22
Phase B healthy (°C)	286	234	52
SC turn (°C)	451	339	112
Hotspot (°C)	610	442	168

D. Fault Behavior under F4

Fault F4 is one turn SC with 3-phase terminal SC at 4000 rpm. Fig. 8 shows the current and the copper loss variations of different winding parts with simulation steps (time). Step zero is healthy condition and fault condition begins from the step 1. It can be observed that when the fault occurs, the currents and losses change rapidly from the healthy values initially and vary slightly during the first a few steps, reaching steady state afterwards. This indicates that the EM-thermal coupled temperature effect on the resistances, currents and on the losses as well on the steady-state temperatures under F4 is insignificant. The observation is, indeed, confirmed by similar temperature distributions predicted by the EM-thermal coupled simulation and by the thermal-only simulation.
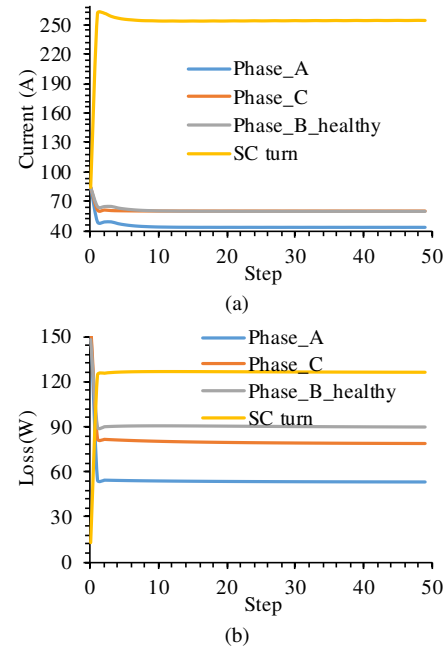

(a)

(b)

Fig. 8. Current and loss variations with simulation step (time). (a) Currents. (b) Losses.
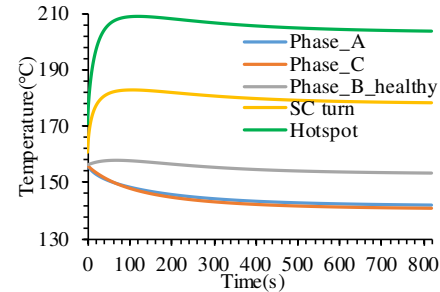

Fig. 9. Transient temperature responses of different winding parts and hotspot.

Fig. 9 shows the transient temperature responses of different winding parts and hotspot during the simulation. It shows that the temperatures of phases A and C are similar despite the current and loss of phase C is higher in Fig. 8. This is because SC turn is more close to the phase A than phase C that

transferring more loss to the phase A. Moreover, the temperatures of phases A and C decrease with time while the temperature of the SC turn and hotspot increase significantly initially due to the increase in the turn loss and decrease slightly afterwards because of the reduction of the copper loss in the healthy part of the phase B coil. The temperature of the healthy part of phase B increases slightly initially because of the larger loss in the SC turn, and then decreases to the value below that in the healthy operation because of the reduction in the copper loss in the healthy part of the phase B coil. The steady state hotspot temperature is greater than that in the healthy operation, but it is below the permissible limit of 220°C. Thus, it shows that the machine is safe under F4 in respect of the thermal behavior.

E. Fault Detection Time under One Turn Short Circuit

It is seen that the hotspot temperature in the SC turn under one turn SC fault (F2) is many times greater than the permissible temperature 220°C of the winding insulation. Thus, three-phase terminal SC must be taken as the mitigation measure for the F2 or F3 fault to reduce the hotspot temperature below the limit. It is important to find the maximum time that is allowed for the fault detection and mitigation. To this end, the EM-thermal coupled simulation is performed again under F2 but with a short time step of 0.05s over 49 steps. The resultant transient hotspot temperature is shown in Fig. 10 and it reaches 220°C at 1.35s. This is the maximum permissible time for fault detection and mitigation.

The effect of the fault mitigation action, i.e., terminal SC via the inverter, applied at 1.35s is also simulated with the EM-thermal coupled model in 0.05s time step and plotted in Fig. 10. As can be seen, the hotspot temperature increases rapidly and reaches just below 220°C at 1.35s. After the application of the mitigation measure, it decreases immediately and rapidly. The time to reach the hotspot temperature of 220°C predicted by the thermal-only simulation is 1.44s but the actual hotspot temperature at this time will reach 226°C. The typical fault detection and inverter response time is within 1s, so the improvement of prediction of the maximum permissible time for the fault detection and mitigation by EM-thermal coupled simulation is less significant.
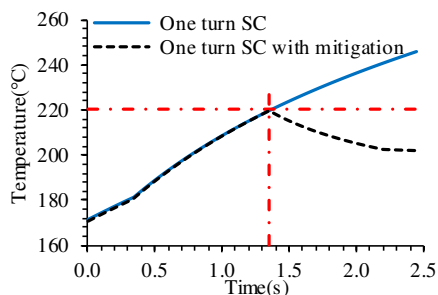

Fig. 10. Hotspot temperature under one turn SC before and after mitigation.

IV. COMPARISON OF PREDICTIONS BY 2D EM AND 3D THERMAL MODELS WITH MEASUREMENTS

The prototype PMASynRM has been built and tested for validation. The machine is mounted on the test rig as in Fig. 11,

employing the oil cooling system as shown in Fig. 12. The cooling oil is fed via the inlet and outlet connections seen in Fig. 12 (b) and circulates in the cooling channel shown in Fig. 12 (a). In addition, one single turn is brought out from the winding by the thick cables as shown in Fig. 13 (a). The fault emulation cables are connected to a high current relay shown in Fig. 13 (b) to emulate and control the inter-turn fault. During manufacturing, the geometry tolerances and material deterioration were reported. This together with the additional impedance of the cable affects the machine performance.

Since the inter-turn SC fault without mitigation measure will result in permanent damage to the prototype, the test is operated under one turn SC at 1000rpm with 40A current excited in the phases for 0.2s. The measured current waveforms will be compared with the predictions by the 2D EM model. Then, the tests are performed under healthy condition and F4 (one turn SC with 3-phase terminal SC) when the machine operates at 4000 rpm and excited with 120A current in the healthy 3-phase sets for 2 hours. The current waveforms predicted by the 2D EM model under F4 condition will be compared with the measurements. Moreover, as discussed in section III, the EM-thermal coupled simulation is not essential but would be more time consuming under F4 condition. Hence the measured temperatures will be compared with the predictions by the 3D thermal-only model under F4 as well as healthy condition.

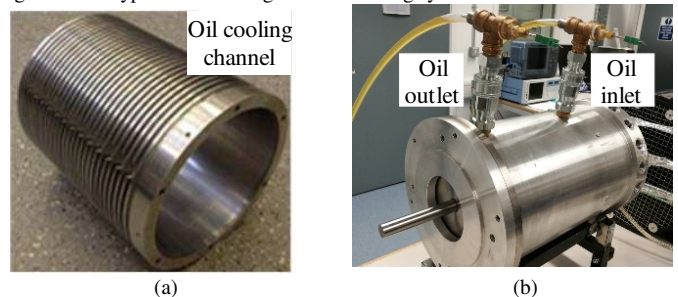Fig. 11. Prototype on the test rig with oil cooling system.

(a)

(b)

Fig. 12. Oil cooling syetem (a) cooling jacket (b) Assembly.
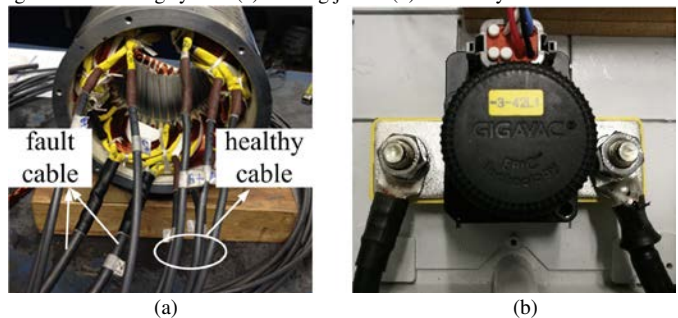

(a)

(b)

Fig. 13. Machine winding leads and relay for turn fault. (a) Leads. (b) Relay.

A. One Turn SC at 1000rpm with 40A Current

The test is under one turn SC without terminal SC fault at 1000rpm with 40A current excited in all the phases for maximum torque per Ampere (MTPA) operation for 0.2s. Fig. 14 and Fig. 15 show the comparison of predicted and measured turn fault current and phase currents in the fault set. As observed from Fig. 14, the predicted turn fault current matches well with the measured turn fault current waveform. The RMS value of the predicted turn fault current which is quite important for thermal analysis is only different from the measured value by 4.4%. As the ideal current sources are adopted in the FE model, all the phases currents are ideally sinusoidal under one turn SC without terminal SC fault. The measured phase currents in the two healthy 3-phase sets are also quite sinusoidal, while the measured phase currents in the fault set are slightly distorted which is not captured by the FE model as shown in Fig. 15 leading to the small difference of the turn fault current.
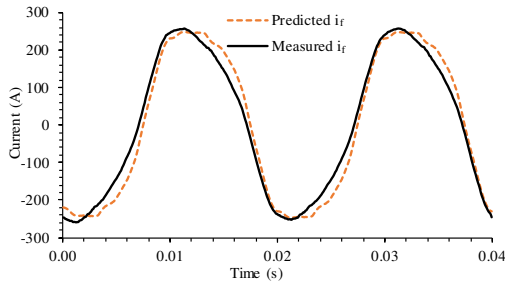

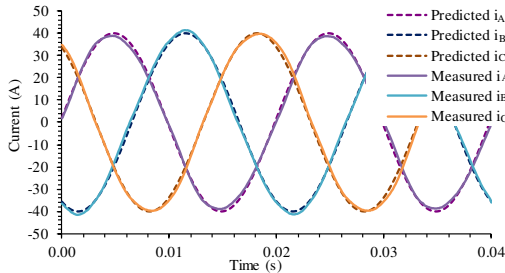Fig. 14. Comparison of predicted and measured turn fault current.

Fig. 15. Comparison of predicted and measured phase currents in fault set.

B. Healthy Condition with 120A

Then the test is performed under healthy condition at 4000 rpm and excited with 120A current for MTPA operation for 2 hours. The inlet and outlet oil temperatures, the coolant volume flow rate, and the temperatures at six different positions in the windings are measured in the test. As the temperature distribution should be the same in each 3-phase set under healthy condition, the 1/3 3D thermal model in Fig. 3 is adopted in simulation. The 3D thermal model considers copper loss variation with temperature, non-uniform end winding layout, the time-dependent oil temperature and coolant volume flow rate, etc. Among the six temperature sensors, two sensors, denoted as tf_ew and tf_slot, are placed in the end winding and slot region of the faulted turn in coil B2 shown in Fig. 2 (a) as the black quadrangle. The two sensors, denoted as b1_slot and e2_slot are placed in the middle of slots of coils B1 and E2, respectively. The other two remaining sensors, denoted as set1_ew and set2_ew are placed in the middle of the end

windings of the ABC and DEF 3-phase sets, respectively. However, the positions of these sensors are not exact.

Since the exact positions of the thermal sensors are not known, the minimum, average and maximum temperatures of the same region predicted by the 3D thermal model are extracted and compared with the measured results in Table IV. Moreover, the values in the last row indicate the difference between the measured and the minimum or the maximum predicted temperatures when the measured temperature is outside the predicted minimum and maximum range.

The measured temperature by sensor set2_ew is higher than the maximum predicted temperature by 3°C. The measured temperature by sensor tf_slot is lower than the minimum predicted temperature by 13°C. The measured temperatures by sensors set1_ew, tf_ew, b1_slot and e2_slot are all between the minimum and maximum predicted temperatures.

TABLE IV
COMPARISONS OF MEASURED AND PREDICTED TEMPERATURES UNDER HEALTHY CONDITION WITH 120A

Temperature (°C)	End winding			Active winding		
	set2_ew	set1_ew	tf_ew	b1_slot	tf_slot	e2_slot
Measured	155	144	139	117	113	117
Predicted max	152	152	152	136	141	140
Predicted min	107	107	137	104	126	95
Predicted average	140	140	146	125	136	130
Difference	3	--	--	--	-13	--

C. One Turn SC with 3-phase terminal SC at 4000rpm with 120A Current

After applying the mitigation measure of 3-phase terminal SC to set ABC, the turn fault current reduces significantly. Therefore, the prototype could be tested under one turn SC with 3-phase terminal SC at 4000 rpm and excited with 120A current in the two healthy 3-phase sets for MTPA operation for 2 hours.

Fig. 16 shows the comparison of predicted and measured phase and turn fault currents in 3-phase set ABC when 120A current is excited in the healthy phases. The predicted turn fault current waveform is very similar to the measured waveform. The difference of RMS values between the predicted and measured turn fault currents is 4.7%. The error is also due to the inaccurate predictions of phase currents of 3-phase set ABC as shown in Fig. 16. However, because the design measures employed for the fault mitigation, the RMS phase currents in the ABC phases are quite low. Consequently, the inaccurate prediction of phase currents of 3-phase set ABC has small effect on the thermal analysis. It can be concluded that the 2D EM model has reasonable accuracy in predicting currents and losses under various fault conditions.
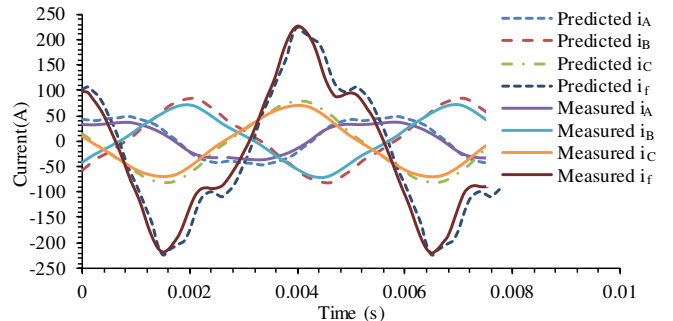

Fig. 16. Comparison of predicted and measured phase and turn fault currents.

From Fig. 16, the current in the faulted turn is ~2.1 pu and the total copper loss of the faulty 3-phase set is 3.5 times lower than that in the healthy 3-phase sets. Due to the asymmetric loss distribution, the full 3D thermal model which comprises 36 slots and 1/2 part of axial length as shown in Fig. 17 is used for accurate thermal analysis. The predicted temperature distribution illustrated in Fig. 18 shows that the two healthy sets have similar temperature distribution and their overall temperature is higher than that of the faulty set. Furthermore, the hotspot located in the middle part of the end windings of the healthy 3-phase sets, because of the much larger copper loss in the healthy 3-phase sets.
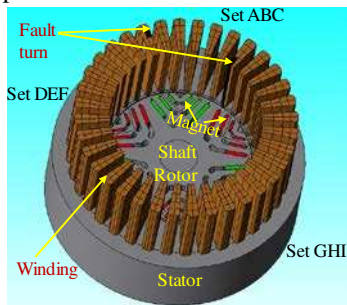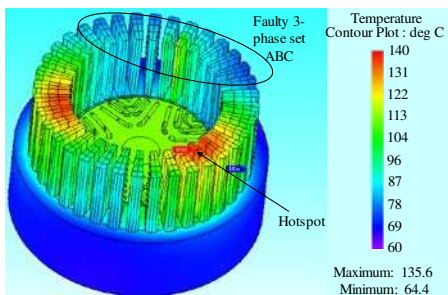

Fig. 17. Full 3D thermal model.

Fig. 18. Temperature distribution under fault condition at 4000rpm.

Table V compares the steady state temperatures obtained by the predictions and measurements. It is worth noting that although the current in the faulted turn is ~2.1 pu as shown in Fig. 16, the temperatures in the fault turn measured by sensors tf_ew and tf_slot are much lower than those in the healthy 3-phase sets measured by sensors set2_ew and e2_slot. This is because the total copper loss in the faulted coil after the mitigation action is much lower than those in the healthy 3-phase sets.

As can be observed, most of the measured temperatures are within the predicted minimum and maximum range. However, the measured temperature of set2_ew is 8°C higher than the maximum predicted temperature. A similar trend is seen from Table IV and Table V that the measured temperatures by sensor set2_ew in the end winding region of the DEF 3-phase set are both larger than those by sensor set1_ew in the end winding region of the ABC set. This may be due to the fact that the sensor position in the DEF set is close to the star-neutral connection which introduces extra resistance and loss, and hence higher temperature. In addition, the measured temperature of tf_slot is also 2°C lower than the minimum predicted temperature which is the same with that in Table IV. It is possible that the position of the sensor has been moved

toward the tooth where the temperature is lower. The measured and predicted temperatures in other positions match well.

Fig. 19 compares the predicted and measured transient temperatures in the end winding region closed to sensor tf_ew. As observed, the measured temperature agrees quite well with the predicted minimum. The comparisons show that the 3D thermal model is quite accurate.

TABLE V
COMPARISONS OF MEASURED AND PREDICTED TEMPERATURES UNDER FAULT CONDITION WITH 120A

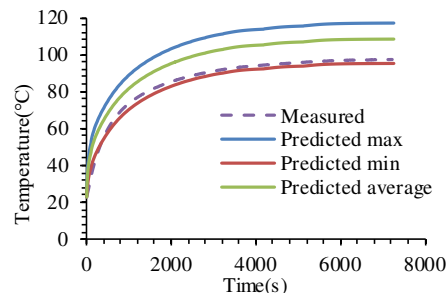| Temperature (°C)	End winding			Active winding		
	set2_ew	set1_ew	tf_ew	b1_slot	tf_slot	e2_slot
Measured	143	91	97	75	89	107
Predicted max	135	99	117	91	104	123
Predicted min	92	72	95	73	90	78
Predicted average	124	85	108	83	102	113
Difference	8	--	--	--	-2	--

Fig. 19. Comparison of predicted and measured transient temperatures in the end winding region close to sensor tf_ew.

V. DISCUSSION

The results of the study show that under F4 the temperatures predicted by thermal only simulation does not differ significantly from those of EM-thermal coupled simulation. This is because the machine loss in the fault region is under effective control and hence the temperature increase is relatively small. While this demonstrates the effectiveness of the mitigation for the machine under study, the condition cannot be assumed true generally. For example, if a design or mitigation measure is less effective in managing the fault, the fault current may be much high and the thermal only simulation may significantly underestimate the hot spot temperature.

Hence, EM-thermal coupled simulation is necessary for assessing fault behavior of a machine in design stages when fault current is inductance limited and the resultant heating effect is very significant. The scenario is very much dependent on design and mitigation measures employed. To our knowledge, there is no quantitative rule-of-thumb technique to determine whether thermal-only simulation is adequate without performing EM-thermal coupled simulation first.

For assessing the fault behaviors without mitigation, EM-thermally coupled simulation is necessary. This type of simulation will be useful to evaluate how long the machine can survive for example. Clearly, complete damage to insulation will occur at temperature significantly greater than the thermal index temperature, and the rate of change of temperature will be significantly underestimated in thermal-only simulation.

Likewise, when the fault current is resistance limited, the thermal only simulation will overestimate the hot spot temperature. Again, if it is necessary to assess more accurately

how long the machine can survive under this fault condition, EM-thermal couple simulation will be necessary.

It should be noted that there is no knowledge in public domain as to how quickly the temperature in the fault region will increase and hence how quick a fault detection and mitigation needs to respond. The results of our study show that the response time is in seconds and that the difference predicted by the thermally only and EM-thermal coupled simulations appears to be small. However, this may not be true for other machines. For surface-mounted PM machines for example, the torque is produced by PM flux only, and hence the back-emf per turn may be ~ 3 times greater than the machine under study. Consequently, the fault current can be ~3 times greater and the resultant heating effect will be 9 times high. In this case, thermal only simulation will incur significant error in prediction. Likewise, if the thermal time constant of the faulted region is small, the temperature rise could be much quick and hence EM-thermal coupled simulation may also be necessary.

VI. CONCLUSION

This paper has performed EM-thermal coupled simulation of a triple redundant, 9-phase PMASynRM with aid of a scripting file. The predicted temperatures by the EM-thermal coupled simulation have been comprehensively compared with those by thermal-only simulation under various faults. It has been shown that at low speed (resistance/reactance limited) or under one turn SC with 3-phase terminal short circuit conditions, the EM-thermal coupled simulation can improve accuracy slightly. However, it is essential to employ the EM-thermal coupled simulation when the fault current is reactance limited at high speed for the study of the thermal behavior under SC fault conditions. The EM-thermal coupled simulation has predicted the maximum permissible time for fault detection and mitigation in the worst case. Measurements on the prototype machine have validated the 2D EM model and the 3D thermal model.

It has also been shown that one turn SC is more severe thermally than two turns SC in this machine because of much larger fault current and hence greater heat intensity in the SC turn.

While the temperatures under F4 predicted by the thermal only and EM-thermal coupled simulations do not differ significantly, this case may not generally be true if the fault current is much greater and the heating effect is more significant, as discussed in section V. In general, it is prudent to perform EM-thermal coupled simulation first to assess if thermal only simulation can be used without significant compromise in accuracy.

REFERENCES

[1] X. Zhu, Z. Xiang, L. Quan, W. Wu and Y. Du, "Multimode optimization design methodology for a flux-controllable stator permanent magnet memory motor considering driving cycles," *IEEE Trans. Ind. Electron.*, vol. 65, no. 7, pp. 5353-5366, Jul. 2018.

[2] M. Popescu, DG. Dorrell, L. Alberti, N. Bianchi, et al., "Thermal analysis of duplex three-phase induction motor under fault operating conditions, " *IEEE Trans. Ind. Appl.*, vol. 49, no. 4, pp. 1523-1530, July/Aug. 2013.

[3] Q. Lu, X. Zhang, Y. Chen, X. Huang, et al., "Modeling and Investigation of Thermal Characteristics of a Water-Cooled Permanent-Magnet Linear Motor," *IEEE Trans. Ind. Appl.*, vol. 51, no. 3, pp. 2086-2096, May/June. 2015.

[4] S. Ruoho, J. Kolehmainen, J. Ikaheimo, and A. Arkkio, "Interdependence of Demagnetization, Loading, and Temperature Rise in a Permanent-Magnet Synchronous Motor, " *IEEE Trans. Magn*, vol. 46, no. 3, pp. 949-953, Mar. 2010.

[5] J. Daesuk, C. Ju-Hee, W. Kyungil, K. Byung-Taek, and K. Dae-kyong, "Electromagnetic Field and Thermal Linked Analysis of Interior Permanent-Magnet Synchronous Motor for Agricultural Electric Vehicle, " *IEEE Trans. Magn*, vol. 47, no. 10, pp. 4242-4245, Oct. 2011.

[6] X. Sun, M. Cheng, S. Zhu, and J. Zhang, "Coupled Electromagnetic-Thermal-Mechanical Analysis for Accurate Prediction of Dual-Mechanical-Port Machine Performance, " *IEEE Trans. Ind. Appl.*, vol. 48, no. 6, pp. 2240-2248, Nov/Dec. 2012.

[7] X. Zhang, W. Li, B. Kou, J. Cao, H. Cao, C. Gerada, et al., "Electrothermal Combined Optimization on Notch in Air-Cooled High-Speed Permanent-Magnet Generator, " *IEEE Trans. Magn*, vol. 51, no. 1, pp. 1-10, Jan. 2015.

[8] J. Wang, W. Wang, K. Atallah, and D. Howe, "Design of a linear permanent magnet motor for active vehicle suspension, " IEEE International Electric Machines and Drives Conference (IEMDC'09), pp. 585-591, 2009.

[9] Y. Shi, J. Wang, and Bo Wang, "EM-thermal coupled simulation under various fault conditions of a triple redundant 9-phase PMASynRM," *10th Energy Conversion Congress and Exposition. ECCE 2018.*

[10] Bo Wang, J. Wang, and B. Sen, et al, " A Fault-Tolerant Machine Drive Based on Permanent Magnet-Assisted Synchronous Reluctance Machine," *IEEE Trans. Ind. Appl.*, vol. 54, no. 2, pp. 1349–1359, Mar./Apr. 2018.

[11] JMAG. [Online]. Available: www.jmag-international.com.

[12] Y. Shi, and J. Wang, "Continuous demagnetization assessment for triple redundant 9-phase fault-tolerant permanent magnet machine," *2018 9th IET Int. Conf. Power Electron. Mach. Drives. PEMD 2018.*

[13] S. Xue, W. Q. Chu and Z. Q. Zhu, et al. "Iron loss calculation considering temperature influence in non-oriented steel laminations," *IET Science, Measurement &* Technology, vol. 10, no. 8, pp. 846–854, Nov. 2016.

[14] Motor-CAD. [Online]. Available: www.motor-design.com.

[15] A. Boglietti, A. Cavagnino and D. Staton, et al. " Evolution and modern approaches for thermal analysis of electrical machines," *IEEE Trans. Ind. Electron.*, vol. 56, no. 3, pp. 871–882, Mar. 2009.

[16] W. Jiang, and T. M. Jahns. "Coupled electromagnetic–thermal analysis of electric machines including transient operation based on finite-element techniques," *IEEE Trans. Ind. Appl.*, vol. 51, no. 2, pp. 1880-1889, Mar/Apr. 2015.

[17] D. P. Kulkarni, G. Rupertus, and E. Chen, "Experimental investigation of contact resistance for water cooled jacket for electric motors and generators," *IEEE Trans. Energy Convers.*, vol. 27, no. 1, pp. 204–210, Mar. 2012.

[18] Z. Hashin and S. Shtrikman, "A variational approach to the theory of the effective magnetic permeability of multiphase materials," *Journal of applied Physics*, vol. 33, no. 10, pp. 3125–3131, Oct. 1962.

[19] L. Idoughi, X. Mininger, and F. Bouillault, et al. "Thermal model with winding homogenization and FIT discretization for stator slot," *IEEE Trans. Magn.*, vol. 47, no. 12, pp. 4822–4826, Dec. 2011.

[20] N. Simpson, R. Wrobel, and P. H. Mellor, "Estimation of equivalent thermal parameters of impregnated electrical windings," *IEEE Trans. Ind. Appl.*, vol. 49, no. 6, pp. 2505–2515, Nov/Dec. 2013.

[21] Y. Shi, J. Wang, and Bo Wang, "Performance assessment of triple redundant 9-phase delta and wye connected Permanent Magnet-assisted Synchronous Reluctance Motor under healthy and fault conditions," *2018 9th IET Int. Conf. Power Electron. Mach. Drives. PEMD*